Texas A&M University

Mechanical Engineering Department

Turbomachinery Laboratory

HYBRID TILTING PAD GAS BEARINGS: ANALYSIS and EXPERIMENTAL VALIDATION

Research Progress Report to the Turbomachinery Laboratory

TRC-B&C-1-05

by

Luis San Andrés

Principal Investigator

May 2005

HYBRID TILTING PAD GAS BEARINGS: ANALYSIS AND EXPERIMENTAL VALIDATION

TRC-B&C-1-05

EXECUTIVE SUMMARY

Gas film bearings offer unique advantages enabling successful deployment of high-speed micro-turbomachinery. Current applications encompass micro power generators, air cycle machines and turbo expanders. Mechanically complex gas foil bearings are in use; however, their excessive cost and lack of calibrated predictive tools deter their application to mass-produced oil-free turbochargers, for example. The present investigation advances the analysis and experimental validation of hybrid gas bearings with static and dynamic force characteristics desirable in high-speed turbomachinery. These characteristics are adequate load support, good stiffness and damping coefficients, low friction and wear during rotor startup and shutdown, and most importantly, enhanced rotordynamic stability at the operating speed.

Hybrid (hydrostatic/hydrodynamic) flexure pivot-tilting pad bearings (FPTPBs) demonstrate superior static and dynamic forced performance than other geometries as measured in a high speed rotor-bearing test rig operating to a top speed of 100 krpm. A computational model including the effects of external pressurization predicts the rotordynamic coefficients of the test bearings and shows good correlation with measured force coefficients, thus lending credence to the predictive model. In general, direct stiffnesses increase with operating speed and external pressurization; while damping coefficients show an opposite behavior. Predicted mass flow rates validate the inherent restrictor type orifice flow model for external pressurization. Measured coast down rotor speeds demonstrate very low-friction operation with system time constants on the order of 60 seconds. Estimated drag torques from the gas bearings validate indirectly the recorded rotor-bearing system time constant.

TRC-B&C-1-05

TABLE OF CONTENTS

LIST OF TABLES

LIST OF FIGURES

Nomenclature

C_P	Nominal clearance [m]
$C_{\alpha\beta_R}$, K_{α,β_R}	Reduced bearing damping and stiffness $_{\alpha,\beta=X,Y}$ [N/m, Ns/m]
$C^S_{\alpha\beta}$, $K^S_{\alpha\beta}$	Pad structure damping and stiffness coefficients $_{\alpha,\beta=\delta,\xi,\eta}$
$C_{\theta\theta}$	Bearing rotational drag coefficient [N.s.m/rad]
D, L	Journal diameter and axial length [m], $R=D/2$
e_X, e_Y	Journal (rotor) eccentricity displacements [m]
F_{pX}, F_{pY}, M_P	Pad fluid film reaction forces and moment [N, N, Nm]
h	Film thickness [m]
$\dot{m}_{OR}$	Orifice mass flow rate [kg/s]
M_R, I_{PR}	Rotor mass [kg] and polar mass moment of inertia [kgm^2]
m_P, I_P	Pad mass [kg] and mass moment of inertia [kgm^2]
P, P_s, P_{or}, P_a	Gas film, Supply, orifice and ambient pressures [Pa]
$\overline{P}$	P_{or}/P_s. Orifice pressure ratio
$P_X, P_Y, P_\xi, P_\eta, P_\delta$	First-order (perturbed) dynamic pressures [Pa/m or Pa/rad]
R_g	Gas constant [J/kg-K]
r_p	Pad preload (m)
T	Gas temperature (K)
W_X, W_Y	External loads acting on rotor [N] (-4.08 N, 0 N)
$x=R\,\theta$, z	Circumferential and axial coordinates [m]
X, Y	Inertial coordinate system fixed to seal center.
$Z_{\alpha,\beta}$	$K_{\alpha,\beta} + i\,\omega\,C_{\alpha,\beta}$, Pad impedance coefficients, $_{\alpha,\beta=X,Y,\delta,\xi,\eta}$
α	Orifice non-isentropic loss coefficient
δ, ξ, η	Pad rotation [rad], radial and transverse displacements [m]
κ	gas specific heat ratio [=1.4]
ρ	P/R_gT. Ideal gas density (kg/m^3)
τ	$I_{RP}/(2\,C_{\theta\theta})$. Time constant [s]
μ	Gas viscosity [Pa-s]
θ	Circumferential coordinate [rad].
Θ_l, Θ_t	Pad leading and trailing angles [rad]
Θ_P	Pad offset angular location [rad]
Ω, ω	Journal speed [rad/s], excitation (whirl) frequency [rad/s]

Subscripts

α,β	X, Y, δ, ξ, η. Direction of dynamic perturbations
P, N_{pad}	Pad number, Number of pads
o	Equilibrium or zeroth order

MATRICES

$[M_p],[K^S_P]$	Pad inertia, Pad structural stiffness
$[Z]$	Pad fluid film impedance matrix, $_{\alpha,\beta=X,Y,\delta,\xi,\eta}$
$[Z_{XY}],[Z_a],[Z_b],$ $Z_c]$	Sub matrices of *[Z]*, Eqn. (23)
$[Z]_R$	$[K]_R + i\,\omega\,[C]_R$ Matrix of frequency reduced force coefficients; $_{\alpha,\beta=X,Y}$ [N/m]

Introduction

Micro-turbomachinery demands gas bearings to ensure compactness, lightweight and extreme temperature operation. Gas bearings with large stiffness and damping, and preferably of low cost, will enable successful commercial applications. Current applications encompass micro power generators, air cycle machines and turbo expanders. Mechanically complex gas foil bearings are in use; however, their excessive cost and lack of calibrated predictive tools deter their application to mass-produced oil-free turbochargers, for example.

Gas film bearings, unlike oil-lubricated bearings, offer advantages of low friction and less heat generation. These advantages enable their successful applications in air-cycle units for airplanes, high-precision instruments, auxiliary power units, and high-speed micro-turbomachinery. In addition, gas bearing systems do not require costly, complex sealing and lubricant circulation systems. Furthermore, these oil-free bearing applications eliminate process fluid contamination and are environmental friendly.

Our main objective is to advance the technology of gas film bearings for applications to oil-free turbomachinery by demonstrating their rotordynamic performance, reliability and durability. References [1-4] detail the research progress to date. Wilde and San Andrés [1,2] describe rotordynamic measurements and analyses conducted on a small rotor supported on three lobed hybrid gas bearings. For various imbalance conditions, coast down tests from 60,000 rpm characterize the rotor response supported on the bearings. As the supply pressure rises, the rotor response shows an increase in critical speed and a noticeable reduction in damping ratio. Threshold speeds of instability also increase with increasing supply pressures, and whirl frequency ratios range from nearly 50% of rotor speed for a purely hydrodynamic condition to 25 % for a pressure supply five times ambient.

Zhu and San Andrés [3] investigate the dynamic forced performance of the same test rotor supported on hybrid flexure pivot - tilting pad bearings (FPTPBs). The bearings demonstrate stable performance and ability to carry dynamic loads up to 99 krpm (limit of the drive motor). Although the FPTPBs are mechanically complex and costlier than cylindrical plain bearings, their enhanced stability characteristics and predictable rotordynamic performance are desirable for high speed turbomachinery applications. Experimental rotor responses show that feed pressure increases the bearings' direct stiffness and critical speed while the viscous damping ratio decreases. Predictions correlate favorably with experimentally identified synchronous direct stiffness, though test damping force coefficients are smaller. Tests without feed pressure show the rotor becomes unstable at ~ 81 krpm with a whirl frequency ratio of 20%. The instability caused the rotor to rub and burn its protective Teflon coating.

Zhu and San Andrés [4] conducted similar experiments of the test rotor supported on Rayleigh step gas bearings, which exhibited adequate stiffness and damping capability in a narrow range of shaft speeds, up to ~ 20 krpm. Severe instabilities ensued at a nearly fixed whirl frequency (system natural frequency) and with very large magnitude subsynchronous amplitude motions that prevented rotor operation above ~ 20 krpm. A

near-frictionless carbon (NFC) coating was applied on the rotor to reduce friction at liftoff and touchdown. However, the rotor could not lift easily and severe rubbing occurred at shaft speeds below ~ 4 krpm. The Rayleigh step gas bearings are the most unreliable rigid bearing configuration tested to date.

Gas bearings, however, have a very low load carrying capacity and require of minute film thickness to accomplish their intended function. Thus, their fabrication and installation tends to be expensive and time consuming. Other disadvantages include little damping because of the gas inherently low viscosity. The provision of pressurized gas during start-up and shutdown periods is desirable to avoid transient rubs and reduce wear. A hybrid bearing configuration offers the combination of hydrostatic and hydrodynamic effects on the bearing static and dynamic forced performance. External pressurization provides supplemental direct stiffness for operation at all rotor speeds and decreases the journal eccentricity. Thus, a hybrid mode operation ultimately results in reduced power consumption. Incidentally, infamous disadvantages stem from two types of instabilities: pneumatic hammer controlled by the flow versus pressure lag in the pressurized gas feeding system, and hydrodynamic instability, a self-excited motion characterized by subsynchronous (forward) whirl motions [5, 6]. A properly designed hybrid bearing system aids to minimize these two kinds of instabilities.

Tilting pad bearings can eliminate the typically harmful hydrodynamic instability by not generating cross-coupled stiffness coefficients. Critical turbomachinery operating well above its critical speeds is customarily implemented with tilting pad bearings. Note that the multiplicity of parameters associated with a tilting pad bearing demands complex analytical methods for predictions of force coefficients and stability calculations [6, 7].

Although tilting pad bearings are not prone to induce subsynchronous instabilities; their time-accumulating drawbacks, namely pad wear and flutter and loss of nominal clearance, result in poor performance in the long run. The flexure pivot – tilting pad bearing (FPTPB) offers a marked improvement over the conventional design since its wire EDM construction renders an integral pads-bearing configuration, thus eliminating pivot wear and stack up of tolerances on assembly. Reference [8] describes the EDM process to fabricate this bearing type, with successful industrial applications given in [9, 10] and demonstrating FPTPBs have a larger load capacity and lower lubricant temperature raise than conventional tilting pad bearings.

Predictive models for liquid lubricated FPTPBs are well known, for example see references [11, 12]. Czolczynsk [13] provides a comprehensive review of gas bearing applications and the numerical analysis for prediction of frequency dependent force coefficients. San Andrés and students [14, 15] advance finite element and finite difference analyses of gas bearings with numerically stable algorithms for accurate dynamic force performance prediction into very high speeds and minute clearances.

The current investigation focuses on flexure pivot – tilting pad gas bearings (FPTPBs). This bearing type is a one-piece mechanical component fabricated with the electric discharge machining (EDM) process. Each pad connects to the bearing through a thin flexural web, which provides a low rotational stiffness, thus ensuring small cross-coupled stiffness coefficients and avoiding subsynchronous instabilities into very high speed operation [3]. FPTPBs also eliminate tolerance stack-up during manufacturing and assembly, as reduce pad wear and pivot contact stresses.

The current work investigates experimentally the dynamic forced performance of a rotor supported on gas FPTPBs supplied with pressurized air, i.e. a hybrid bearing configuration. Rotor dynamic displacements and bearing transmitted forces are measured during coast-down tests to baseline and calibrated imbalance masses. Run-up tests are conducted to high speeds in search of regions of rotordynamic unstable response regions. The bearings stiffness and damping coefficients are estimated from the measured responses. Predicted stiffness and damping coefficients are in close agreement with the identified bearing coefficients.

Analysis of hydrostatic/hydrodynamic gas film bearing

Figure 1 shows a flexure pivot-tilting pad gas bearing, a one-piece mechanical component EDM fabricated. Figure 2 depicts a schematic view of a tilting pad with its relevant nomenclature. Each pad connects to the bearing through a thin flexural web, which provides a low rotational stiffness, thus ensuring small cross-coupled stiffnesses and avoiding subsynchronous instabilities into very high speed operation. For operation with external pressurization, a feed orifice is machined through the thin web.
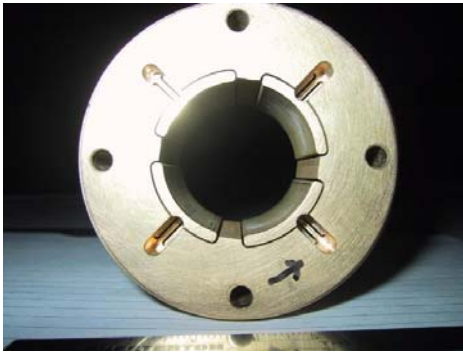
Fig. 1 Flexure pivot tilting pad – gas bearing for oil-free test rig

The journal rotates at speed (Ω) and (e_X, e_Y) denote the journal displacements within the bearing clearance. The film thickness (h) is described relative to the coordinate system ($x=R\cdot\theta$, y). Each pad extends from Θ_l to Θ_t (leading and trailing edge angular coordinates) with three degrees of freedom corresponding to angular (tilt) rotation (δ_p), radial (ξ_p) and transverse displacements (η_p). The support web, modeled as an elastic structure with viscous type damping, provides reaction moments (M_P) and forces (F_ξ, F_η)$_P$. Pitching motions along the axial direction are not accounted for. The film thickness on a pad is

$$h = C_p + e_X \cos\theta + e_Y \sin\theta + (\xi_p - r_p)\cos(\theta - \Theta_p) + (\eta_p - R\delta_p)\sin(\theta - \Theta_p) \qquad (1)$$

where C_P and r_p are the nominal clearance and pad preload at the offset $\varTheta_P$ angle where the web is attached.
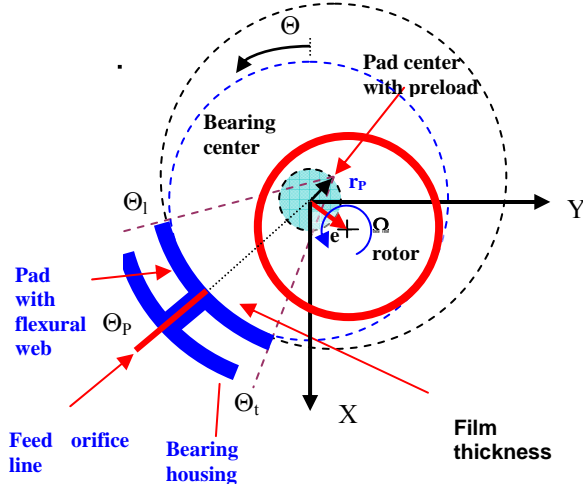
Fig. 2 Geometry of a flexure-pivot pad with orifice for external pressurization

In an ideal gas undergoing an isothermal process, the density and pressure are related by $\rho = \dfrac{P}{\Re_g \cdot T}$, with $\Re_g$ and T representing the gas constant and operating temperature, respectively. The Reynolds equation for an ideal gas describes the inertialess and isoviscous flow within the thin film. This equation establishes the balance of pressure and shear driven mass flow rates and the mass flow rate ($\dot m_{OR}$) from an external pressure source, i.e.

$$\nabla \cdot \left(\frac{-h^3 P}{12\mu} \cdot \nabla(P) \right) + \frac{\Omega \cdot R}{2} \cdot \frac{\partial}{\partial x}(Ph) + \frac{\partial}{\partial t}(Ph) = 0 \qquad (2)$$

The pressure is ambient (P_a) on the sides ($z=0, L$) of a bearing pad, The orifice mass flow rate, $\dot m_{OR}$, depends on the pressure ratio $\overline{P} = P_{or}/P_s$ the orifice diameter (d) and the local film thickness (h), i.e. from [16],

$$\dot m_{OR} = \pi\, d\, h\, \frac{P_s}{\sqrt{\Re_g T}} \cdot \Phi(\overline{P}) \qquad (3)$$

with
$$\Phi_{(\overline{P})} = \left| \begin{array}{l} \left(2 \cdot \dfrac{\kappa}{\kappa+1} \right)^{1/2} \cdot \left(\dfrac{2}{\kappa+1} \right)^{1/{k-1}} \quad for \quad \overline{P} \langle\, \overline{P}_{choke} = \left(\dfrac{2}{\kappa+1} \right)^{k/{k-1}} \\[2ex] \alpha' \cdot \left(2 \cdot \dfrac{\kappa}{\kappa-1} \right)^{1/2} \cdot \overline{P}^{1/k} \cdot \left(1 - \overline{P}^{k-1/k} \right)^{1/2} \quad for \quad \overline{P} \rangle\, \overline{P}_{choke} \end{array} \right. \qquad (4)$$

where κ is the gas specific heat ratio, and (α') is a non-isentropic loss coefficient. Thus, the flow restriction is of inherent type with flow control strongly affected by the local film thickness.

Perturbation analysis of thin film flow equations

An applied external static load (W_o) determines the rotor equilibrium position $(e_X, e_Y)_o$ with steady pressure field P_o and film thickness h_o, and corresponding pad deflections $(\delta_P,\ \xi_P,\ \eta_P)_{o,\ P=1,...Npad}$. Let the journal whirl with frequency ω and small amplitude motions $(\Delta e_X,\ \Delta e_Y)$ about the equilibrium position. The general motion of the rotor center and pads is expressed as,

4

$$e_X = e_{Xo} + \Delta e_X \, e^{i\omega t}, \quad e_Y = e_{Yo} + \Delta e_Y \, e^{i\omega t}, \qquad \xi_p = \xi_{po} + \Delta \xi_p \, e^{i\omega t}, \quad i = (1)^{1/2}$$

$$\eta_p = \eta_{po} + \Delta \eta_p \, e^{i\omega t}, \quad \delta_p = \delta_{po} + \Delta \delta_p \, e^{i\omega t} \qquad\qquad p = 1,2,...,N_{pad} \qquad\qquad (5)$$

The film thickness and hydrodynamic pressure are also given by the superposition of equilibrium (zeroth order) and perturbed (first-order) fields, i.e.

$$h = h_o + \Delta h \, e^{i\omega t} \qquad ; \qquad P = P_o + \Delta P \, e^{i\omega t} \qquad\qquad (6)$$

where

$$\Delta h = \Delta e_X \cos\theta + \Delta e_Y \sin\theta + \Delta \xi_P \cos(\theta - \Theta_P) + \left(\Delta \eta_P - R\,\Delta\delta_P \right) \sin(\theta - \Theta_P) \qquad (7)$$

and

$$\Delta P = \left\{ P_X \, \Delta e_X + P_Y \, \Delta e_Y + P_\delta \, \Delta\delta_P + P_\xi \, \Delta\xi_P + P_\eta \, \Delta\eta_P \right\} \qquad (8)$$

Substitution of (6) into the Reynolds equation (2) leads to a nonlinear PDE for the equilibrium pressure (P_o) and five linear PDEs for the first-order fields, i.e.

$$\frac{1}{R^2} \frac{\partial}{\partial\theta} \left(\frac{P_o \cdot h_o^3}{12 \cdot \mu} \frac{\partial P_o}{\partial\theta} \right) + \frac{\partial}{\partial z} \left(\frac{P_o \cdot h_o^3}{12 \cdot \mu} \frac{\partial P_o}{\partial z} \right) = \frac{\Omega}{2} \frac{\partial}{\partial\theta} \left(P_o \cdot h_o \right) \qquad (9)$$

with

$$h_o = C_p + \left(\xi_{po} - r_p - e_{\xi o} \right) \cos(\theta - \Theta_p) + \left(\eta_{po} - R\,\delta_{po} - e_{\eta o} \right) \sin(\theta - \Theta_p) \qquad (10)$$

and

$$e_{\xi o} = -e_{Xo} \cos\Theta_p - e_{Yo} \sin\Theta_p \,, \quad e_{\eta o} = e_{Xo} \sin\Theta_p - e_{Yo} \cos\Theta_p \qquad (11)$$

as the components of the rotor center displacement along the radial and transverse (ξ, η) pad *local* coordinates. Define the linear differential operators,

$$\ell(P_\alpha) = \frac{1}{R^2} \frac{\partial}{\partial\theta} \left(\frac{P_o \cdot h_o^3}{12 \cdot \mu} \frac{\partial P_\alpha}{\partial\theta} \right) + \frac{\partial}{\partial z} \left(\frac{P_o \cdot h_o^3}{12 \cdot \mu} \frac{\partial P_\alpha}{\partial z} \right) \qquad (12a)$$

$$\ell_f(f_\alpha) = \left[\frac{1}{R^2} \frac{\partial}{\partial\theta} \left(\frac{P_o f_\alpha \cdot 3h_o^2}{12 \cdot \mu} \frac{\partial P_o}{\partial\theta} \right) + \frac{\partial}{\partial z} \left(\frac{P_o f_\alpha \cdot 3h_o^2}{12 \cdot \mu} \frac{\partial P_o}{\partial z} \right) \right] \qquad (12b)$$

$$\ell_P(P_\alpha) = \left[\frac{1}{R^2} \frac{\partial}{\partial\theta} \left(\frac{P_\alpha \cdot h_o^3}{12 \cdot \mu} \frac{\partial P_o}{\partial\theta} \right) + \frac{\partial}{\partial z} \left(\frac{P_\alpha \cdot h_o^3}{12 \cdot \mu} \frac{\partial P_o}{\partial z} \right) \right] \qquad (12c)$$

and the **first-order equations** for each perturbed pressure field are:

$$\ell(P_X) = \left(\frac{\Omega}{2} \frac{\partial}{\partial\theta} + i\omega \right) \left[P_o \cos\theta + h_o \, P_X \right] - \ell_f(\cos\theta) - \ell_P(P_X) \qquad (13a)$$

$$\ell(P_Y) = \left(\frac{\Omega}{2} \frac{\partial}{\partial \theta} + i\omega \right) \left[P_o \sin\theta + h_o P_Y \right] - \ell_f(\sin\theta) - \ell_P(P_Y) \tag{13b}$$

$$\ell(P_{\xi_P}) = \left(\frac{\Omega}{2} \frac{\partial}{\partial \theta} + i\omega \right) \left[P_{\xi_P} \cos(\theta - \Theta_P) + h_o P_{\xi_P} \right] - \ell_f(\cos(\theta - \Theta_P)) - \ell_P(P_{\xi_P}) \tag{13c}$$

$$\ell(P_{\eta_P}) = \left(\frac{\Omega}{2} \frac{\partial}{\partial \theta} + i\omega \right) \left[P_{\eta_P} \sin(\theta - \Theta_P) + h_o P_{\eta_P} \right] - \ell_f(\sin(\theta - \Theta_P)) - \ell_P(P_{\eta_P}) \tag{13d}$$

$$\ell(P_{\delta_P}) = \left(\frac{\Omega}{2} \frac{\partial}{\partial \theta} + i\omega \right) \left[-P_{\delta_P} R\sin(\theta - \Theta_P) + h_o P_{\eta_P} \right] + \ell_f(R\sin(\theta - \Theta_P)) - \ell_P(P_{\delta_P}) \tag{13e}$$

The first-order pressure fields satisfy homogeneous conditions, i.e. $P_\alpha=0$; thus it immediately follows that the pressure fields due to radial (ξ_P), transverse (η_P), and angular (δ_P) motions of the p-th pad are:

$$P_\delta = R[P_X \sin\Theta_p - P_Y \cos\Theta_p] \;; P_\eta = [-P_X \sin\Theta_p + P_Y \cos\Theta_p] \; ; \text{and}$$

$$P_\xi = [P_X \cos\Theta_p + P_Y \sin\Theta_p] \tag{14}$$

Thus, the first-order fields above are not calculated numerically but directly determined using (P_X, P_Y) after solving Eqns. (13a-b). Clearly, savings in computational time are exceptional.

Perturbations to the orifice flow equation are also derived but not given here for brevity. For details on the analysis see references [14, 15]

The equilibrium pressure field acting on the rotor surface generates film reaction forces from each pad (F_{pX}, F_{pY}),

$$\begin{bmatrix} F_{pX} \\ F_{pY} \end{bmatrix} = \int\int (P - P_a) \begin{bmatrix} \cos\theta \\ \sin\theta \end{bmatrix} R\, d\theta\, dz \tag{15}$$

These forces (with opposite sign) also act on each pad and induce a pitching moment (M_P),

$$M_P = R[F_{pX} \sin\Theta_P - F_{pY} \cos\Theta_P] \tag{16}$$

Substitution of the pressure fields, zeroth and first order, into the pad force and moment equations leads to:

$$\begin{Bmatrix} F_{pX} \\ F_{pY} \\ M_p \end{Bmatrix} = \begin{Bmatrix} F_{pXo} \\ F_{pYo} \\ M_{po} \end{Bmatrix} - \begin{bmatrix} Z_{XX} & Z_{XY} & Z_{X\delta} & Z_{X\xi} & Z_{X\eta} \\ Z_{YY} & Z_{YX} & Z_{X\delta} & Z_{X\xi} & Z_{Y\eta} \\ Z_{\delta X} & Z_{\delta Y} & Z_{\delta\delta} & Z_{\delta\xi} & Z_{\delta\eta} \end{bmatrix} \begin{Bmatrix} \Delta e_X \\ \Delta e_Y \\ \Delta \delta_P \\ \Delta \xi_P \\ \Delta \eta_P \end{Bmatrix} e^{i\omega t} \tag{17}$$

where
$$Z_{\alpha\beta} = \{K_{\alpha\beta} + i\omega C_{\alpha\beta}\}, \quad \alpha\beta = X,Y,\delta,\xi\eta \tag{18}$$

represent the gas film impedances acting on each pad, i.e. 25 stiffness and damping coefficients. Reference [15] details the specific formulae for each fluid film impedance coefficient.

An external load with components *(W_X, W_Y)*, comprising a static part *(W_o)* and a dynamic part *(ΔW e^{iωt})*, acts on the rotor and is transmitted through the pads to the bearing. The pad film reaction forces balance the applied load according to the equations:

$$W_X = W_{Xo} + \Delta W_X e^{j\omega t} = -\sum_p F_{pX} \qquad W_Y = W_{Yo} + \Delta W_Y e^{j\omega t} = -\sum_p F_{pY} \qquad (19)$$

The moment and force equations governing the angular *(δ_p)*, radial *(ξ_p)* and transverse *(η_p)* motions for each pad are [10]:

$$[M_p]\begin{Bmatrix} \ddot{\delta}_P \\ \ddot{\xi}_P \\ \ddot{\eta}_P \end{Bmatrix} + [K_P^S]\begin{Bmatrix} \delta_P \\ \xi_P \\ \eta_P \end{Bmatrix} + [C_P^S]\begin{Bmatrix} \dot{\delta}_P \\ \dot{\xi}_P \\ \dot{\eta}_P \end{Bmatrix} = \begin{Bmatrix} M_P \\ F_{P_\xi} \\ F_{P_\eta} \end{Bmatrix} \qquad p=1,\ldots N_{pad} \qquad (20)$$

where

$$[M_P] = \begin{bmatrix} I_P & 0 & 0 \\ 0 & m_P & 0 \\ 0 & 0 & m_P \end{bmatrix}, \quad [K_P^S] = \begin{bmatrix} K_{\delta\delta}^S & K_{\delta\xi}^S & K_{\delta\eta}^S \\ K_{\xi\delta}^S & K_{\xi\xi}^S & K_{\xi\eta}^S \\ K_{\eta\delta}^S & K_{\eta\xi}^S & K_{\eta\eta}^S \end{bmatrix}, \quad [C_P^S] = \begin{bmatrix} C_{\delta\delta}^S & C_{\delta\xi}^S & C_{\delta\eta}^S \\ C_{\xi\delta}^S & C_{\xi\xi}^S & C_{\xi\eta}^S \\ C_{\eta\delta}^S & C_{\eta\xi}^S & K_{C\eta\eta}^S \end{bmatrix} \qquad (21)$$

are matrices representing the pad inertias, and the structural web stiffness and viscous damping coefficients, respectively.

Frequency reduced force coefficients for tilting pad bearing

Substitution of Eqn. (17) into (20) leads to a system of differential equations integrating the effects of the gas film and pad structure. Next, an analytical procedure leads to <u>frequency reduced</u> impedance coefficients [17], i.e.

$$[Z]_R = \begin{bmatrix} Z_{XX_R} & Z_{XY_R} \\ Z_{YX_R} & Z_{YY_R} \end{bmatrix} = [K]_R + i\,\omega[C]_R = \sum_P \left([Z_{XY}]_P - [Z_a]_P [Z_{p+f}]^{-1} [Z_b]_P \right) \qquad (22)$$

The matrix $[Z]_R$ contains the frequency reduced stiffness and damping coefficients for rotor lateral motions *(X,Y)*. For rotor imbalance response, synchronous force coefficients are calculated with *ω=Ω*. For eigenvalue rotordynamic analysis, iterative methods allow the determination of the coefficients at frequencies coinciding with the rotor-bearing system natural frequencies. In the equation above,

$$[Z]_P = \begin{bmatrix} Z_{XX} & Z_{XY} & Z_{X\delta} & Z_{X\xi} & Z_{X\eta} \\ Z_{YX} & Z_{YY} & Z_{Y\delta} & Z_{Y\xi} & Z_{Y\eta} \\ Z_{\delta X} & Z_{\delta Y} & Z_{\delta\delta} & Z_{\delta\xi} & Z_{\delta\eta} \\ Z_{\xi X} & Z_{\xi Y} & Z_{\xi\delta} & Z_{\xi\xi} & Z_{\xi\eta} \\ Z_{\eta X} & Z_{\eta Y} & Z_{\eta\delta} & Z_{\eta\xi} & Z_{\eta\eta} \end{bmatrix}_P = \begin{bmatrix} [Z_{XY}]_{2x2} & [Z_a]_{2x3} \\ [Z_b]_{3x2} & [Z_c]_{3x3} \end{bmatrix}_P \tag{23}$$

and
$$[Z_{P+f}] = [K_P^S] + i\omega[C_P^S] + [Z_c] - \omega^2[M_P] \tag{24}$$

is the composite (pad plus film) impedance matrix reduced at frequency ω [18].

An iterative procedure based on the Newton-Raphson method is easily implemented for simultaneous satisfaction of the overall load balance, and the forces and moment balance on each pad. The method was introduced in [12] for the analysis of flexure pivot tilting pad hydrodynamic bearings. The numerically stable method of solution follows the exact procedure introduced in [18]. The method avoids spurious numerical oscillations and allows prediction of gas film static and dynamic characteristics for arbitrarily high-speed gas bearing numbers.

Iterative method for balance of pads at the static load condition
At equilibrium, the bearing overall reaction force must equal the applied load, i.e. $W_X+F_{Xo}=0$, $W_Y+F_{Yo}=0$. The journal equilibrium displacements $\{e_{X_o}, e_{Y_o}\}$ determine the equilibrium pad displacements $\{\delta_o, \xi_o, \eta_o\}_{P; P=1,..,N_{pad}}$, satisfying

$$[K_P^S]\begin{Bmatrix} \delta_{P_o} \\ \xi_{P_o} \\ \eta_{P_o} \end{Bmatrix} = \begin{Bmatrix} M_{P_o} \\ F_{P_{\xi o}} \\ F_{P_{\eta o}} \end{Bmatrix} \tag{25}$$

where $M_{P_o} = f(e_X, e_Y, \delta_P, \xi_P, \eta_P)_o$, etc.

A Newton-Raphson procedure is implemented for simultaneous satisfaction of the overall load balance, and the forces and moment balance on each pad [12, 15]. At the k_{th} iteration, the vectors $\{\delta_P, \xi_P, \eta_P\}^{(k)}$ giving $\{M_P, F_{P\xi}, F_{P\eta}\}^{(k)}$ may not satisfy Eqn. (25), i.e.

$$[K_P^S]\begin{Bmatrix} \delta_P \\ \xi_P \\ \eta_P \end{Bmatrix}^{(k)} - \begin{Bmatrix} M_P \\ F_{P_\xi} \\ F_{P_\eta} \end{Bmatrix}^{(k)} = \{r_P^{(k)}\} \neq 0 \tag{26}$$

Improved pad displacements leading towards a residual $\{r_P^{(k)}\} \rightarrow \{0\}$ on each pad follow as $\delta_P^{(k+1)} = \delta_P^{(k)} + \overline{\Delta}\delta_P$, etc. Assume that $\{\overline{\Delta}\delta_P, \overline{\Delta}\xi_P, \overline{\Delta}\eta_P\}$ are small, and to satisfy Eqn. (25) at the $(k+1)_{\text{th}}$ iteration with an improved pad displacement vector, then

$$[K_P^S]\begin{Bmatrix}\delta_P\\\xi_P\\\eta_P\end{Bmatrix}^{(k)} + [K_P^S]\begin{Bmatrix}\overline{\Delta}\delta_P\\\overline{\Delta}\xi_P\\\overline{\Delta}\eta_P\end{Bmatrix}^{(k)} = \begin{Bmatrix}M_{P_o}\\F_{P_{\xi o}}\\F_{P_{\eta o}}\end{Bmatrix}^{(k)} = \begin{Bmatrix}M_P\\F_{P_\xi}\\F_{P_\eta}\end{Bmatrix}^{(k)} - \begin{bmatrix}K_{\delta\delta}&K_{\delta\xi}&K_{\delta\eta}\\K_{\xi\delta}&K_{\xi\xi}&K_{\xi\eta}\\K_{\eta\delta}&K_{\eta\xi}&K_{\eta\eta}\end{bmatrix}^{(k)}\begin{Bmatrix}\overline{\Delta}\delta_P\\\overline{\Delta}\xi_P\\\overline{\Delta}\eta_P\end{Bmatrix} \quad (27)$$

where $K_{\alpha\beta}$, $\alpha,\beta=\delta,\ \xi,\ \eta$, represents the static film stiffness coefficients on each pad. Eqn. (26) is rewritten as

$$[K_P^S]\begin{Bmatrix}\delta_P\\\xi_P\\\eta_P\end{Bmatrix}^{(k)} - \begin{Bmatrix}M_P\\F_{P_\xi}\\F_{P_\eta}\end{Bmatrix}^{(k)} = \{r_P^{(k)}\} = -\left[[K_P^S]+[K_c]^{(k)}\right]\begin{Bmatrix}\overline{\Delta}\delta_P\\\overline{\Delta}\xi_P\\\overline{\Delta}\eta_P\end{Bmatrix}^{(k)} = -[K_{P+f}^{(k)}]\begin{Bmatrix}\overline{\Delta}\delta_P\\\overline{\Delta}\xi_P\\\overline{\Delta}\eta_P\end{Bmatrix}^{(k)} \quad (28)$$

Thus, the required changes to the vector of pad displacements are determined from

$$\begin{Bmatrix}\overline{\Delta}\delta_P\\\overline{\Delta}\xi_P\\\overline{\Delta}\eta_P\end{Bmatrix}^{(k)} = -\left[K_{P+f}^{(k)}\right]^{-1}\{r_P^{(k)}\} \quad (29)$$

In the process above, the rotor displacements $\{e_X,e_Y\}_o$ remain invariant, while the iterative scheme proceeds to balance the statics equation on each pad. However, the scheme does not ensure the balance of statics load, i.e $(W_o+F_o)_{X,Y}=0$. A similar procedure, say at k_{th} iteration, determines improved rotor eccentricity displacements $\{e_{X,Y}^{(k+1)}=e_{X,Y}^{(k)}+\overline{\Delta}e_{X,Y}^{(k)}\}$, where

$$\begin{Bmatrix}\overline{\Delta}e_X\\\overline{\Delta}e_Y\end{Bmatrix} = \left[[K]_R^{(k)}\right]^{-1}\begin{Bmatrix}\overline{\delta}W_X\\\overline{\delta}W_Y\end{Bmatrix}^{(k)} \quad (30)$$

with $\begin{Bmatrix}\overline{\delta}W_X\\\overline{\delta}W_Y\end{Bmatrix}^{(k)}$ as the residual vector in static forces. Above,

$$[K]_R^{(k)} = \sum_P \left([K_{XY}]_P - [K_a]_P [K_{P+f}]^{-1} [K_b]_P\right)^{(k)} \quad (31)$$

is the matrix of reduced static stiffness coefficients. Note that these stiffness coefficients are evaluated at null excitation frequency.

Description of test rig and bearings

Figure 3 depicts the test rig with a steel main body integrating a brushless electric motor armature (top speed 100 krpm). The motor drives a rotor supported on two identical flexure pivot pad gas bearings, shown in detail in Figure 4. References [1-4] detail the test rig components, AC motor integral to the rotating shaft, and the design and operating envelope of the test bearings.
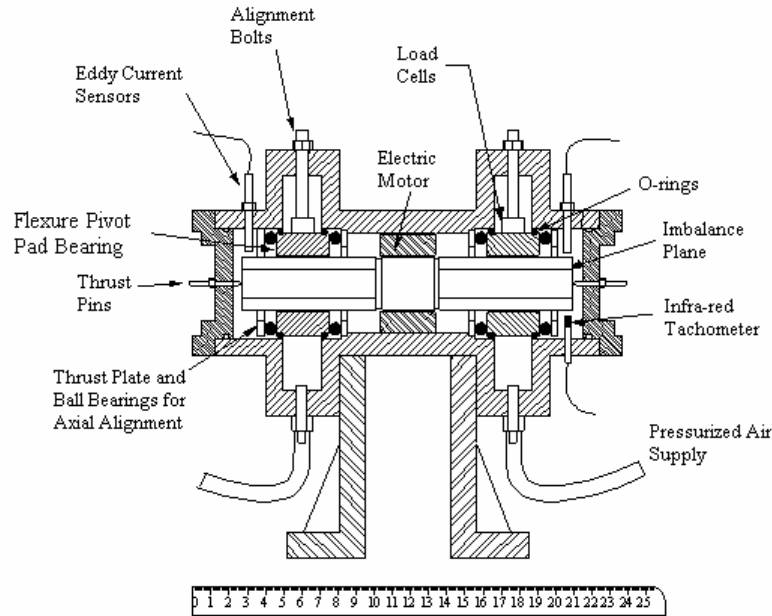

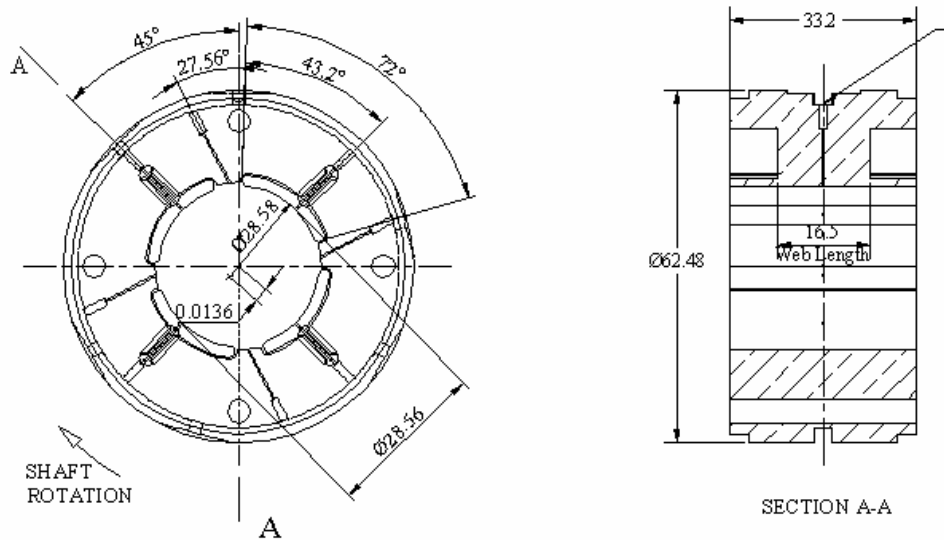**Fig. 3 Schematic cross section view of gas bearing test rig (Unit: cm)**

Fig. 4 Dimensions of flexure pivot – hydrostatic bearing

10

Table 1 presents the test bearings geometry, each with four pads and 60% pivot offset. The nominal bearing bore diameter is 28.58 mm with a 0.014 mm machined preload (r_p). The Teflon® coated journal sleeves are 28.500 mm in diameter. Pressurized air flows into the middle plane of each pad through a 0.38 mm diameter orifice. The bearings are installed in the (static) load on pad configuration. The (measured) radial clearance of the bearing is ~ 0.040 mm. The flexure in the bearing provides nearly rigid radial and transverse stiffnesses, i.e. $K_{\xi\xi}^S = K_{\eta\eta}^S \rightarrow \infty$, and the moment stiffness $K_{\delta\delta}^S = 20$ Nm/rad is known from the bearing manufacturer. The static load on each bearing equals 4.05 N and the rotor speed varies from 10 krpm to 100 krpm.

Table 1. Dimensions of test flexure pivot - tilting pad bearing and rotor
(measurements after construction, not designed element)

Parameter	Value	Unit
Rotor mass, M	0.827	kg
Rotor diameter with coating, D_J	28.50 ± 0.001	mm
Bearing bore diameter, D	28.58 ± 0.003	mm
Bearing clearance, c_P	40 ± 4.5	μm
Bearing axial length, L	33.2	mm
Pads number and arc length	4 (72 °)	
Pad pivot offset	60%	
Pad preload, r_P	14	μm
Pad mass, m_P	10.85	gram
Pad mass moment of inertia, I_P	0.253	gram-mm^2
Web rotational stiffness, $K_{\delta\delta}$	20	Nm/rad
Feed orifice diameter	0.62	mm

Design: orifice diameter=0.508 mm, and clearance = 0.020 mm

Operating conditions:
Gas Constant, R_g	286.7 J/Kg-°C (air)
Temperature, T	27 °C
Viscosity, μ	1.85x 10^{-6} Pa-s
Density, ρ_a	1.16 kg/m^3
Ambient pressure, P_a	1.01 bar

Pairs of eddy current sensors, orthogonally positioned and facing the rotor ends, record the shaft motions along the *X-(*vertical*)* and *Y-(*horizontal*)* directions. Three piezoelectric load cells, 120 ° apart, are connected to each bearing for measurement of the transmitted load. Positioning bolts secure the load cells and bearing in place. Zhu and San Andrés [3] describe the coast-down speed tests to record the rotor motions and transmitted bearing loads for various imbalance conditions and three feed absolute pressures, 2.4, 3.8 and 5.1 bars (20, 40 and 60 psig). The imbalance responses show the supply pressure raising the system critical speed (increase in bearing direct stiffness) while the viscous damping ratio decreases, as shown in Figure 5.

Review of measurements and predictions based on hydrodynamic gas film model

In [3], experimentally derived force coefficients, stiffness and damping, are correlated with model predictions based in the analysis given in [15]. Unfortunately, at the time the analysis was conducted, the available computational model was restricted to prediction of dynamic force coefficients in a purely hydrodynamic bearing configuration, i.e. without the effects of the external pressurization and orifice restriction.

Figure 6 shows the experimentally derived and predicted force coefficient for one of the test bearings. Predicted stiffnesses correlate favorably with experimentally identified (synchronous) direct stiffness bearing force coefficients. Experimental damping coefficients are 50% or lower than predicted magnitudes, though remaining relatively constant as the rotor speed increases. Presently, improved predictions with the improved model including the hydrostatic pressurization are obtained, as detailed next.
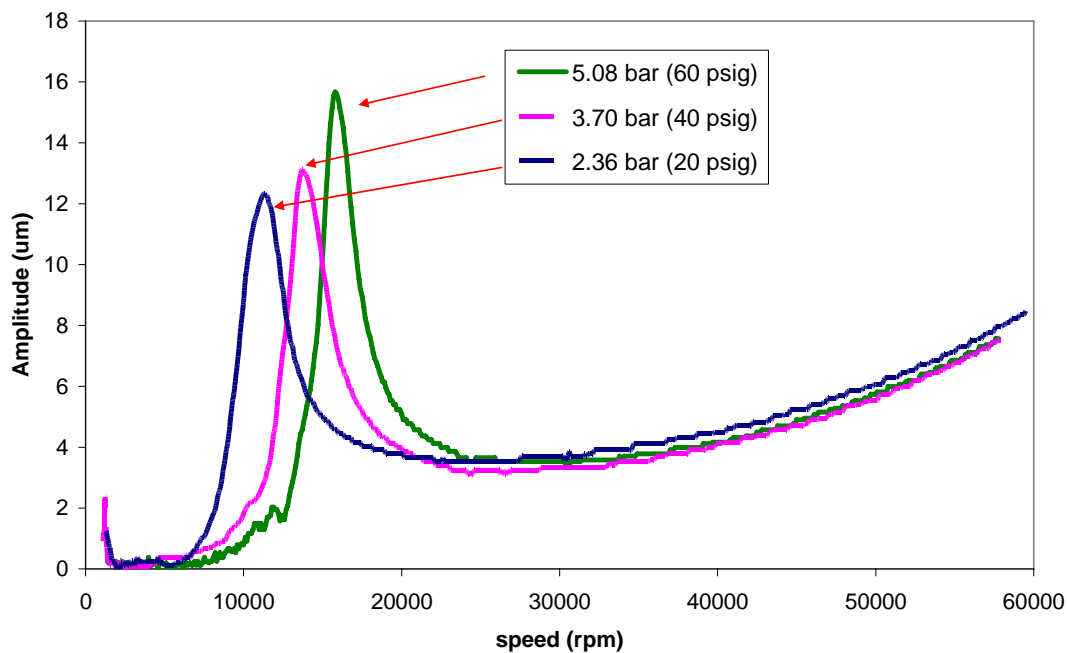

Fig. 5 Measured synchronous amplitude of rotor motion supported on flexure pivot gas bearings. Effect of increasing feed hydrostatic pressurization. Test data recorded at left bearing, vertical plane. Reference [3]
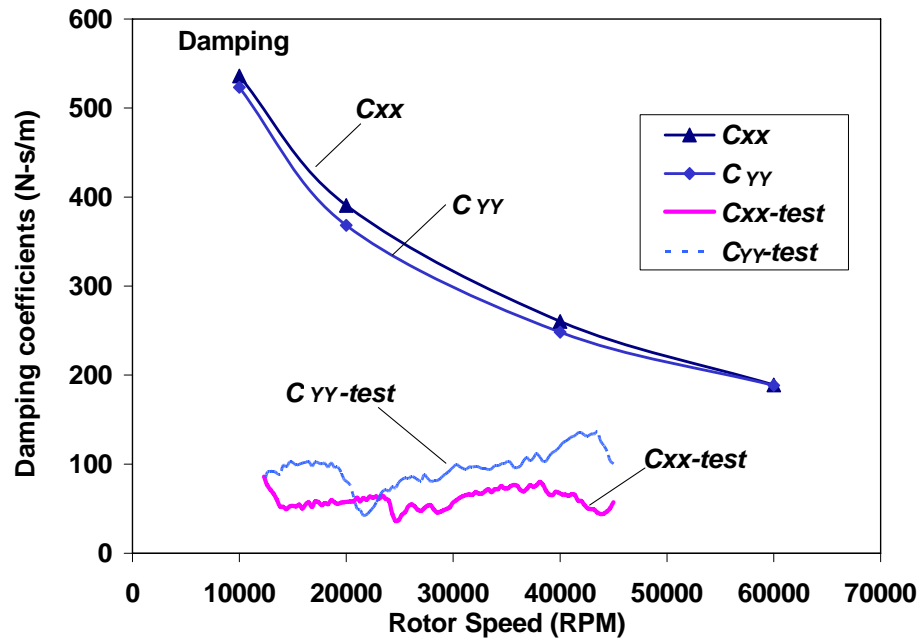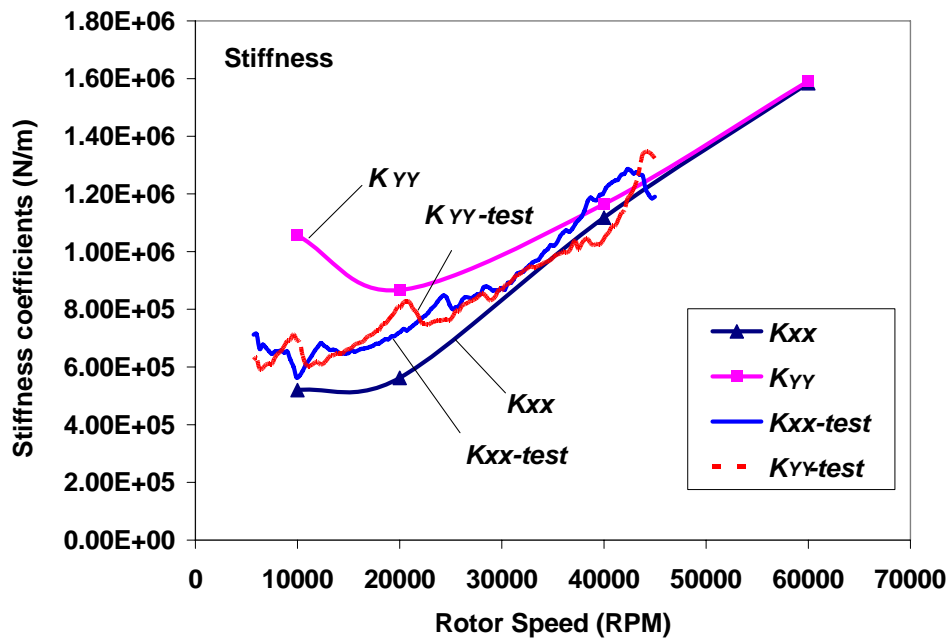
Fig. 6 Comparison of experimentally derived, from [3], and predicted direct stiffness and damping force coefficients for test gas bearing (2.39 bar supply pressure). Predictions based on purely hydrodynamic gas film model [15].

Description of computational program

TILTPADHGB®, acronym for Tilt Pad Hybrid Gas Bearing, is a FORTRAN computer program finding the static and dynamic forced response of multiple pad gas bearings. An EXCEL® graphical user interface handles the user input and output calculations to and from the FORTRAN executable program.

Figure 7 displays the spreadsheet with the major parameters for description of a multiple pad bearing configuration. Each cell has annotated comments providing a description of its contents. The interface offers two major calculation options:
   a) given rotor eccentricity, find reaction forces and force coefficients,
   b) given applied load, find rotor eccentricity and force coefficients.

As user selected options, rotordynamic force coefficients (stiffness and damping) are calculated as synchronous for a range of operating speeds or for a number of whirl frequencies keeping the rotor speed constant. Figure 8 displays in tabular form, as a function of load and rotor speed, the calculated force coefficients and other static performance characteristics, i.e. flow rate, power loss, maximum pressure, etc. The interface creates graphs depicting the variation of the predicted parameters (stiffness and damping coefficients, flow rate, drag torque and power loss) versus rotor speed or whirl frequency (whichever is appropriate).

Predictions from hybrid gas film model and comparison to test results

Numerical predictions were conducted with the improved computational model that includes the external feed pressurization, i.e. hydrostatic effects. Table 1 lists the bearing geometry and operating conditions. In the numerical analysis, each pad is represented by 17 x 11 mesh points in the circumferential and axial directions, respectively. The convergence criteria for pressure convergence is set to 10^{-5} Pa.

<u>Mass flow rate</u> Figure 9 depicts the measured and predicted mass flow rate through each test bearing for increasing supply pressures, 1 to 5 bar. The computed results agree very well with the measurements, demonstrating the accuracy of the inherent orifice flow model. Note that even for the highest feed pressure, the predicted film pressure is not low enough to cause flow choking. This fact was also noted in the experimentation [3].

<u>Steady state eccentricity</u> The fraction of static load acting on each bearing, **4.08 N**, determines the equilibrium position of the journal within its bearing. Figure 10 depicts the predicted journal eccentricity ratio and attitude angle for increasing rotor speeds. As the pressure supply increases, the journal static displacement is smaller denoting a stiffening of the gas bearing. Incidentally, the attitude angle is also reduced bringing the journal displacement towards the load direction. Note that the attitude angle is largest for the pure hydrodynamic condition, showing the flexure pivot bearing rotational stiffness is not negligible.

Experimental data for the static journal position was not identified reliably from the rotor dynamic motions.

Figure 11 depicts the predicted gas pressure (P/P_a) and film thickness (h/C) at the bearing center plane for supply pressure and shaft speed equal to 3.7 bar and 20 krpm, respectively. The figure also includes a depiction of the pressure field acting on the rotor surface. One can easily note the location of the feed pressurization ports.

<u>Stiffness coefficients</u> Direct force coefficients, stiffness and damping, synchronous with shaft speed, were identified in [3] from simple transfer functions obtained from measurements of the shaft displacements and transmitted loads to the rig casing. The identification procedure uses the synchronous components of rotor motion and loads, and relies heavily on the accurate measurement of the phase angle. Large uncertainties are expected while the rotor passes through the critical speed since the rotor/bearing system had very little damping. Reference [3] does not detail the uncertainty in the identified parameters.

Figure 12 shows the direct stiffnesses, K_{XX}, K_{YY}, versus rotor speed for three test pressures. Predictions are depicted for identical pressures and the hydrodynamic condition. Note that the model predictions correctly show the trend of increasing direct stiffness as the shaft speed increases. The best correlation between test results and predictions is for a supply pressure of 2.36 bar (20 psig).

Figure 13 depicts the test derived and predicted direct damping coefficients, C_{XX}, C_{YY}, versus rotor speed. The model damping values are still larger than the identified parameters; however, the trend in reduction in viscous damping as the feed pressure increases is correct. In general, the current model does a better job than the simpler hydrodynamic model used earlier [3].

<u>Coastdown rotor speed</u> Once a rotor lifts on its gas bearings, the drag friction is very small since air has very low viscosity. This is obviously one of the major advantages of gas bearings.

Figure 14 shows the recorded coast down speed of the test rotor versus time. Note the large time, well over 2 minutes, for the rotor to decelerate to rest from a top speed of 60 krpm. Note that increasing the feed pressure tends to increase the overall time of rotor lift off, in particular at very low shaft speeds.

The test data shows that the decay of shaft speed is of exponential type, i.e. due solely to viscous drag effects, for most of the operating speed range. Thus, a simple model of the form,

$$\Omega = \Omega_o \, e^{-t/\tau}, \quad \tau = I_p/(2 \, C_{\theta\theta})$$

where τ is the system time constant and $C_{\theta\theta}$ is a rotational viscous damping coefficient derived from the drag torque in the bearings ($C_{\theta\theta} = T_{orque}/\Omega$) and windage effects from the

motor armature. The experimental time constant for the system ranges from 63 s to 57 s as the supply pressure decreases (average value 60.3 s), while the estimation equals 89 s, as derived from predictions of the drag torque from the bearings (alone). The difference is certainly due to the not quantified drag in the motor. The time constant estimation serves to validate indirectly the prediction of the drag torque in the bearings. A calculated bearing drag friction coefficient, $f=T_{orque}/(R\ W)$, is proportional to shaft speed. This coefficient ranges from 0.007 to 0.01 as the supply pressure increases. Thus, the tested air bearings do offer nearly negligible friction against rotation.

Predictions of rotordynamic response A FE structural model for the test rotor was developed using an in-house rotordynamics software tool [2]. The model replicates very well the free-free elastic modes of the composite rotor and verifies this is nearly rigid within the range of operating shaft speeds, maximum 100 krpm. The predicted synchronous force coefficients for each pressure condition are incorporated into the program for prediction of the rotor imbalance response. Note that gas bearings have frequency dependent force coefficients which must be used in system eigenvalue analysis determining the natural frequencies and damping ratios for stable performance.

Figure 15 depicts predictions of the rotor imbalance response at the left bearing (vertical) plane. The predictions show that feed pressurization increases the system critical speed and reduces the damping ratio. The test results evidenced a similar behavior.

Figure 16 presents the predicted and measured synchronous rotor response for a condition of feed pressure equal to 2.36 bar (20 psig). The correlation of linear rotordynamic predictions to the test data is remarkable. The figure includes the imbalance masses used in the analysis. The actual imbalance is unknown. The one used was determined from matching the peak amplitude of motion at the critical speed.

Conclusions

To date the hybrid flexure pivot-tilting pad bearings (FPTPBs) have demonstrated superior static and dynamic forced performance than simple three-lobe bearings and Rayleigh-step bearings. The FPTPBs are mechanically complex and more expensive; however, their enhanced stability characteristics and predictable rotordynamic performance, with verified operation to speeds as high as 100 krpm, makes them desirable for the envisioned oil-free applications in high speed micro turbomachinery.

A computational model including the effects of external pressurization predicts the rotordynamic coefficients of the test bearings and shows good correlation with measured force coefficients, thus lending credence to the predictive model. In general, direct stiffnesses increase with operating speed and external pressurization; while damping coefficients show an opposite behavior. The rotational structural stiffness of the pad web determines the amount of cross-coupled stiffness coefficients in a FPTPB. Correlation of predicted mass flow rates and measurements also validates the inherent orifice-flow model. Finally, predictions of the drag torque from the gas bearings also verify indirectly

the test measurements which show very long times for coasting down; thus demonstrating a nearly friction-free operation.

Acknowledgments

References

[1] Wilde, D.A., and San Andrés, L., 2003, "Experimental Response of Simple Gas Hybrid Bearings for Oil-Free Turbomachinery," ASME Paper GT 2003-38833.

[2] Wilde, D.A., and San Andrés, L., 2003, "Comparison of Rotordynamic Analysis Predictions with the Test Response of Simple Gas Hybrid Bearings for Oil Free Turbomachinery," ASME Paper GT2003-38859.

[3] Zhu, S. and L., San Andrés, 2004, "Rotordynamic Performance of Flexure Pivot Hydrostatic Gas Bearings for Oil-Free Turbomachinery," ASME Paper GT 2004-53621.

[4] Zhu, S. and L., San Andrés, 2005, "Experimental response of a Rotor Supported on Rayleigh Step Gas Bearings, ASME Paper GT2005-68296.

[5] Lund, J. W., 1967, "A Theoretical Analysis of Whirl Instability and Pneumatic Hammer for a Rigid Rotor in Pressurized Gas Journal Bearings", ASME Journal of Lubrication Technology, Vol. 89, pp. 154-163.

[6] Stowell, T. B., 1971, "Pneumatic Hammer in a Gas Lubricated Externally Pressurized Annular Thrust Bearing", ASME Journal of Lubrication Technology, Vol. 93, pp. 498-503.

[6] Wong, R. Y., Stewart, W. L., and Rohlok, H. E., 1968, "Pivot-Pad Journal Gas Bearing Performance in Exploratory Operation of Brayton Cycle Turbocompressor", ASME Journal of Lubrication Technology, Vol. 90, pp. 687-700.

[7] Lund, J. W., and Pederson, L. B., 1987, "The Influence of Pad Flexibility on the Dynamic Coefficients of a Tilting Pad Journal Bearing", ASME Journal of Lubrication Technology, Vol. 109, pp. 65-70.

[8] Zeidan, F.Y., 1992, "Developments in Fluid Film Bearing Technology," Turbomachinery International, pp. 24-31.

[9] Armentrout, R. W., and Paquette, D. J., 1993, "Rotordynamic Characteristics of Flexure-Pivot Tilting-Pad Journal Bearings", STLE Tribology Transactions, Vol. 36, pp. 443-451.

[10] Chen, W. J., Zeidan, F. Y., and Jain, D., 1994, "Design, Analysis and Testing of High Performance Bearing in a High Speed Integrally Geared Compressor", Proceeding of the 23rd Turbomachinery Symposium, pp. 31-42.

[11] Chen, W.J., 1995, "Bearing Dynamic Coefficients of Flexible-Pad Journal Bearings," STLE Transactions, 38(2), pp. 253-260.

[12] San Andrés, L., 1996, "Turbulent Flow, Flexure-Pivot Hybrid Bearings for Cryogenic Applications," ASME Journal of Tribology, Vol. 118, 1, pp. 190-200.

[13] Czolczynski, K., 1999, "Rotordynamics of Gas-Lubricated Journal Bearing System", Springer Verlag.

[14] San Andrés, L. and D., Wilde, 2001, "Finite Element Analysis of Gas Bearings for Oil-Free Turbomachinery," Revue Européenne des Eléments Finis, Vol. 10 (6/7), pp. 769-790.

[15] Delgado, A., L., San Andrés, and J. Justak, 2004, "Analysis of Performance and Rotordynamic Force Coefficients of Brush Seals with Reverse Rotation Ability", ASME Paper GT 2004-53614.

[16] Mori, H., and Miyamatsu, Y., 1969, "Theoretical Flow-Models for Externally Pressurized Gas Bearings", ASME Journal of Lubrication Technology, Vol. 91, pp. 183-193.

[17] Lund, J. W. 1968, "Calculation of Stiffness and Damping Properties of Gas Bearings", ASME Journal of Lubrication Technology, Vol. 90, pp. 793-803

[18] Faria, M., and L. San Andrés, 2000, "On the Numerical Modeling of High Speed Hydrodynamic Gas Bearings," ASME Journal of Tribology, Vol. 122, 1, pp. 124-130.

XLTiltPadHGB™ worksheet for HYBRID GAS BEARINGS (rigid or tilting pads)

Version 1.0, Copyright 2005 by Texas A&M University. All rights reserved. Dr. Luis San Andres

Title: FLEXURE PIVOT GAS BEARING TAMU - WITH external pressurization - LOAD ON PAD

ISOTHERMAL MODEL

TRC Project 32513/1519 S7

Interface to Program: TltPadHGB

EDIT "DUMP.TXT" after program execution to VERIFY calculation

PHYSICAL Units   S.I.

CONVERGENCE PARAMETERS

HYDROSTATIC PAD CONFIGURATION

			Orifice Loss Coefficient	0.87

				Orifice	Feed Pressure	Diameter	X-loc	Y-loc
Rotor Diameter	0.0285	meters	Max Iterations - film lands	500	--	Vary Load	Select Analysis Type	#	bar	mm	[-]	[-]

Rotor Diameter	0.0285	meters
Axial Length	0.0332	meters
Radial Clearance	3.00E-05	meters
Number of pads on bearing	4	
Pad 1 - arc length	72.00	degrees
Pad 1 -leading edge	46.80	degrees
Preload (dim)	0.20	2.40E-05 min c
Pad 1 - offset (% arc length)	0.60	

Fluid Properties

Ambient pressure	1.01	bar
Gas Spec Heat Ratio	1.4	-
Ambient Temperature	26.7	C
Viscosity at Pambient	1.85E-02	c-Poise
Density at Pambient	1.16	kg/m3

CONVERGENCE PARAMETERS		
Max Iterations - film lands	500	--
error pressure film lands	1.00E-05	

GRID RATIO (circ/Axial)	0.15	
No. Circ. Grid Points	34	Nx
No. Axial Grid Points	10	Ny

X Static Eccentricity Ratio	0.0547	--
Y Static Eccentricity Ratio	0.0242	--
Frequency Analysis Option		
Constant Shaft Rpm	50000	rpm

Synchronous Analysis

Vary Load   Select Analysis Type

Tilting Pads		OPTION - TILTING PAD?	
0.00E+00	Pad mass	kg	
0.00E+00	Pad Inertia	kg-m2	

TILTING or FLEXURE PIVOT PAD Stiffness Matrix

Moment	20	0	0	pad rotation angle
normal F	0	1.00E+08	0	Normal displacement
transverse F	0	0	1.00E+08	Transverse displacement

TILTING or FLEXURE PAD Damping Marrix

Moment	0	0	0	pad rotation velocity
normal F	0	0	0	Normal or radial velocity
transverse F	0	0	0	Transverse velocity

Orifice #	Feed Pressure bar	Diameter mm	X-loc [-]	Y-loc [-]
1	5.149	0.51	19	1
2		0.38		
3	2.392			
4	3.77			
5	5.149			

Fig. 7 Example Input data in worksheet for analysis of tilting pad (hybrid) gas bearing
(**left:** geometry and gas properties, **middle:** parameters for convergence and grid size; **right:** configuration of tilt pads and hydrostatic feed ports)

Load-X N	Load-Y N	Speed rpm	Kxx N/m	Kxy N/m	Kyx N/m	Kyy N/m	Cxx N-s/m	Cxy N-s/m	Cyx N-s/m	Cyy N-s/m
4.056	0	100000	2.67E+06	2.77E+05	-2.42E+05	2.72E+06	1.54E+02	-5.80E+01	6.07E+01	1.55E+02
4.056	0	80000	2.51E+06	3.25E+05	-3.17E+05	2.55E+06	1.57E+02	-5.14E+01	5.43E+01	1.58E+02
4.056	0	60000	2.35E+06	3.09E+05	-3.14E+05	2.37E+06	1.56E+02	-4.14E+01	4.31E+01	1.58E+02
4.056	0	40000	2.15E+06	2.34E+05	-2.36E+05	2.16E+06	1.56E+02	-2.82E+01	2.85E+01	1.58E+02
4.056	0	20000	1.90E+06	1.10E+05	-1.06E+05	1.90E+06	1.60E+02	-1.28E+01	1.24E+01	1.60E+02
4.056	0	10000	1.74E+06	3.58E+04	-2.94E+04	1.74E+06	1.64E+02	-4.63E+00	4.11E+00	1.63E+02

Speed rpm	ex/C [-]	ey/C [-]	Mass Flow kg/s	Fx Reaction N	Fy Reaction N	Power Loss kW	Keq N/m	WFR	Torque N.m	Force N	Angle	Max pressure bar
100000	0.067	0.053	1.61E-04	-4.05	0.03	0.04	2.59E+06	0.16	3.87E-03	4.05E+00	0.0000	2.871
80000	0.070	0.030	1.62E-04	-4.04	-0.02	0.03	2.42E+06	0.24	3.15E-03	4.04E+00	0.0000	2.900
60000	0.068	0.016	1.63E-04	-4.04	-0.01	0.02	2.28E+06	0.31	2.44E-03	4.04E+00	0.0000	2.902
40000	0.068	0.010	1.64E-04	-4.05	-0.01	0.01	2.12E+06	0.36	1.72E-03	4.05E+00	0.0000	2.899
20000	0.074	0.005	1.64E-04	-4.05	-0.01	0.00	1.89E+06	0.32	1.00E-03	4.05E+00	0.0000	2.898
10000	0.079	0.001	1.64E-04	-4.05	-0.01	0.00	1.74E+06	0.19	6.34E-04	4.05E+00	0.0000	2.902

Fig. 8 Example of predictions from analysis of hybrid tilting pad gas bearing
Top-left (gray): operating conditions – speed and load; Top-right (red): predicted force coefficients,
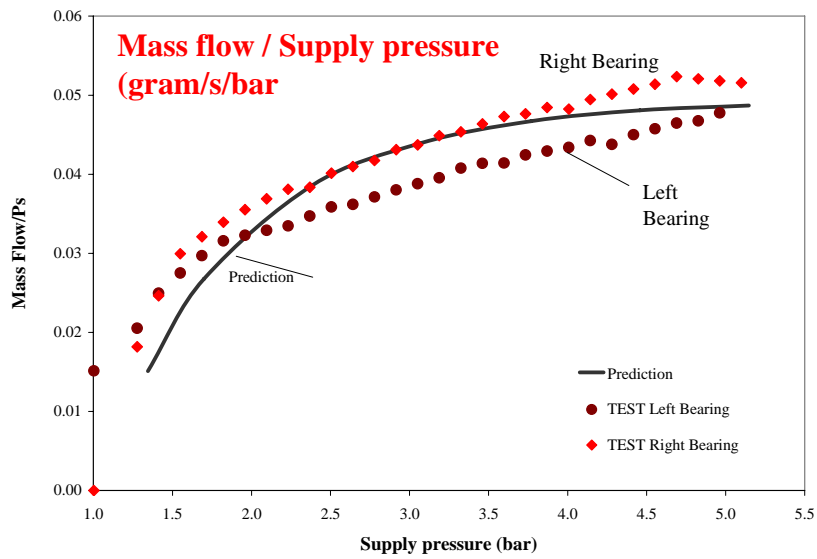Bottom (red): predicted static eccentricity, mass flow, power loss, etc

(a)
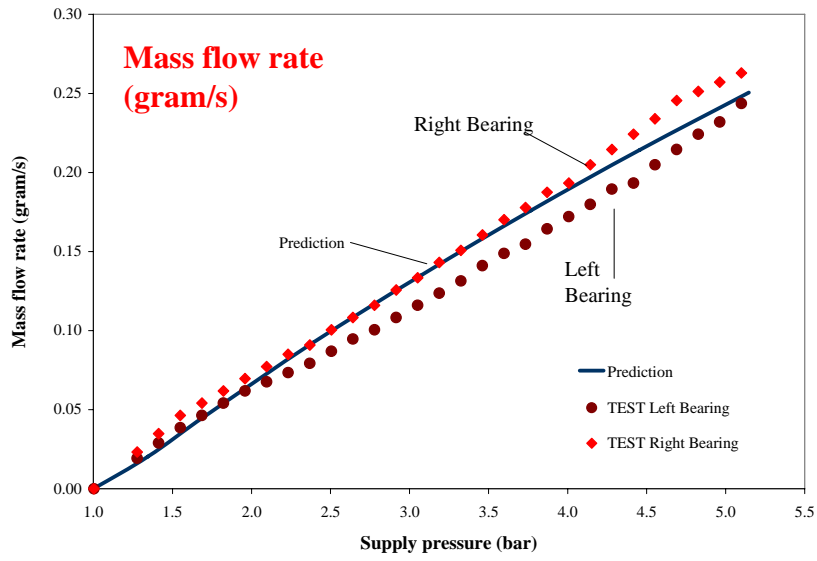
(b)

Fig. 9 Flow rate vs supply pressure for test bearings. Measurements [3] and current predictions. Rotor speeds ranged from 10 to 60 krpm
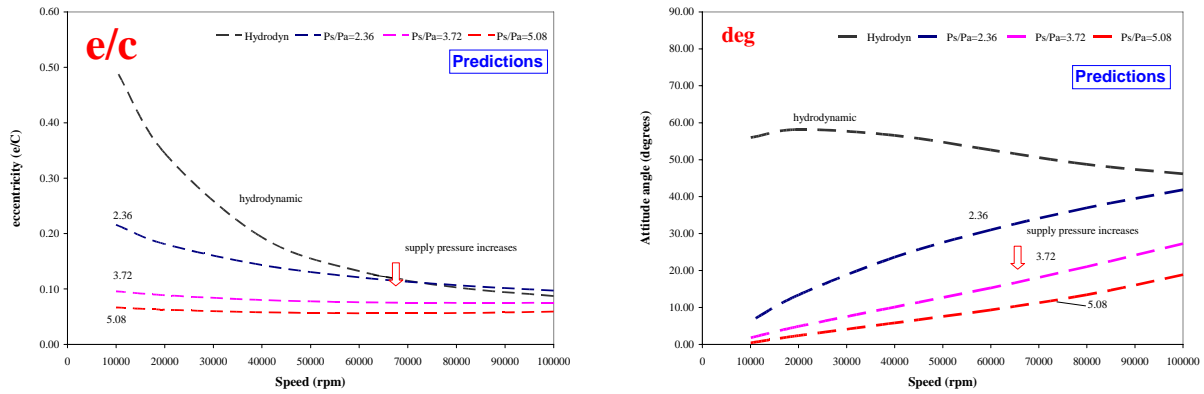
Fig. 10 Predicted static journal eccentricity *(e/c)* **and attitude angle vs rotor speed for increasing supply pressures. Static load** *W***=4.08 N (LOP)**
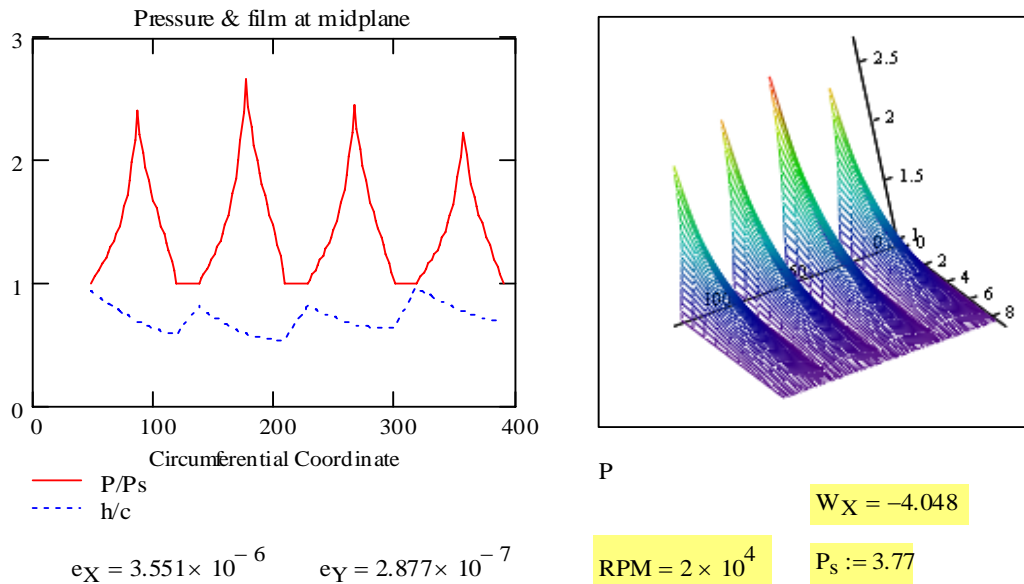

$e_X = 3.551 \times 10^{-6}$ $e_Y = 2.877 \times 10^{-7}$

$W_X = -4.048$

$RPM = 2 \times 10^4$ $P_s := 3.77$

Fig. 11 Predicted pressure field and film thickness for gas bearing operating at 20 krpm and 3.77 bar (60 psig) supply pressure. Static load *W***=4.08 N (LOP)**
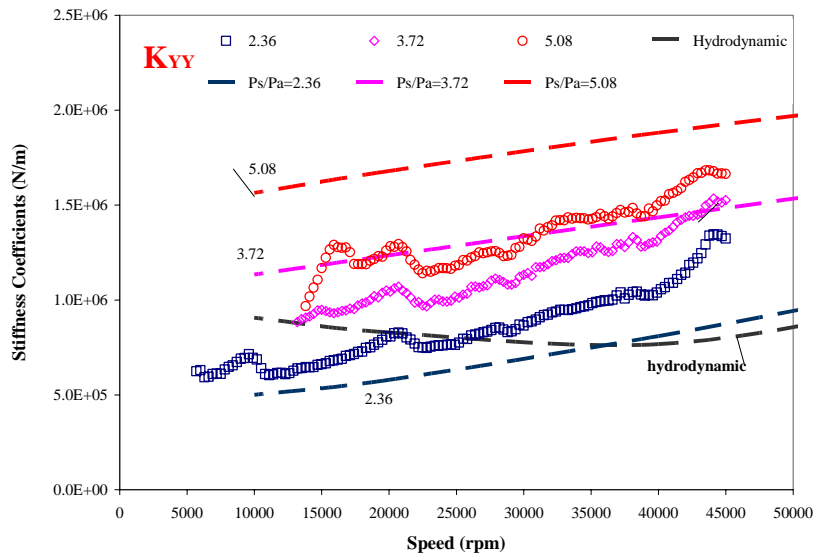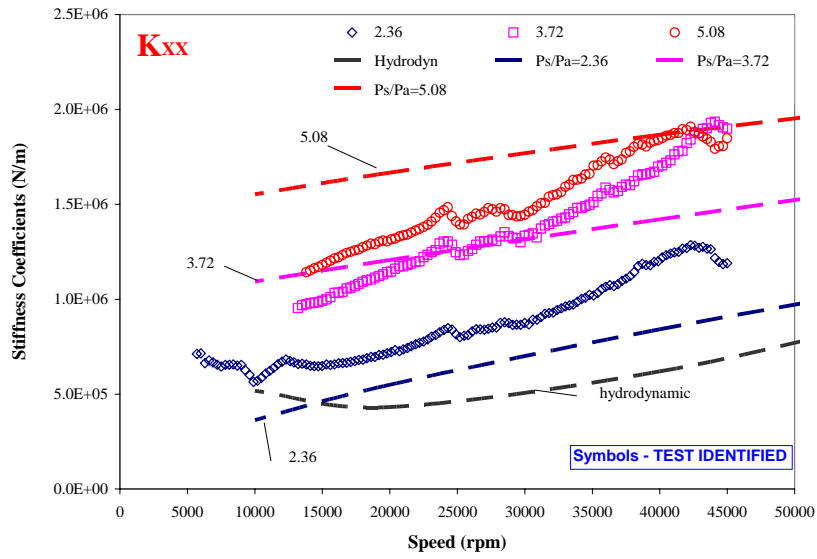
Fig. 12 Bearing direct stiffness coefficients (K_{XX}, K_{YY}) vs rotor speed for three magnitudes of gas supply pressure. Comparison of predictions to identified synchronous force coefficients from measurements
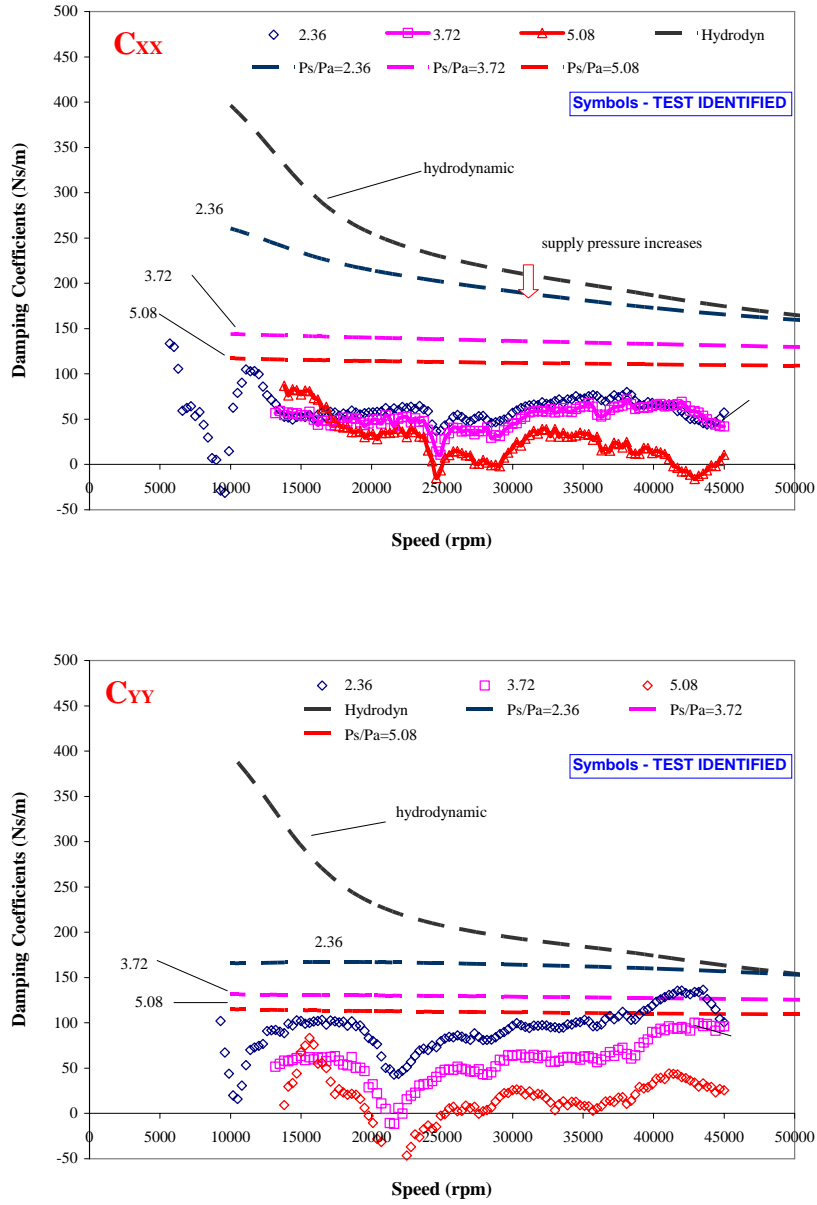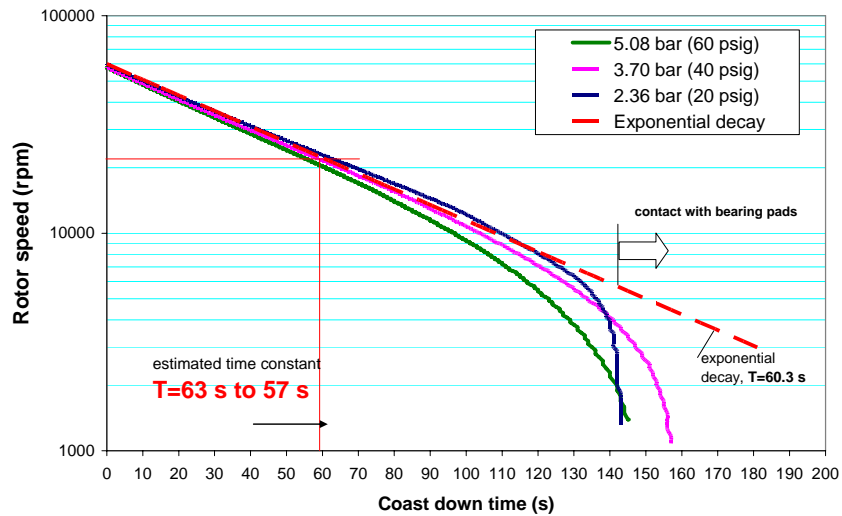
Fig. 13 Bearing direct damping coefficients (C_{XX}, C_{YY}) vs rotor speed for three magnitudes of gas supply pressure. Comparison of predictions to identified synchronous force coefficients from measurements
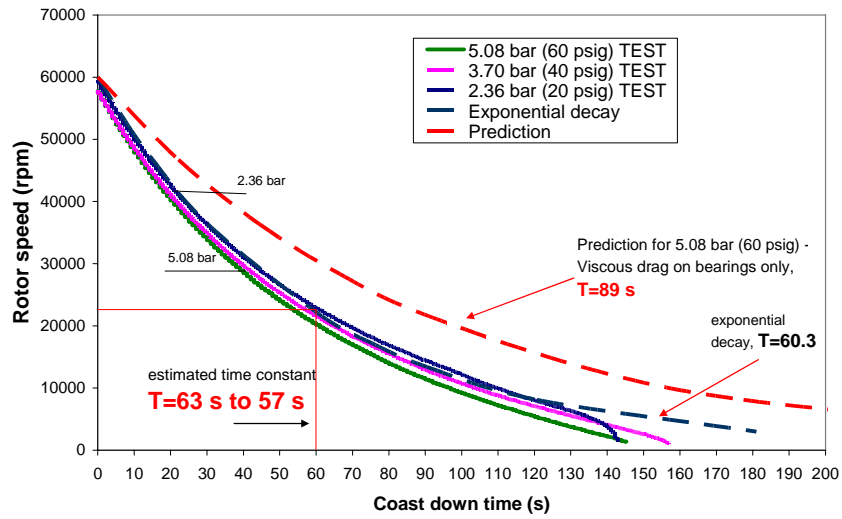
Fig. 14 Recorded coast down rotor speed vs time for three feed pressures (2.36, 3.70 and 5.08 bar). Shaft speed shown in linear and logarithmic scales

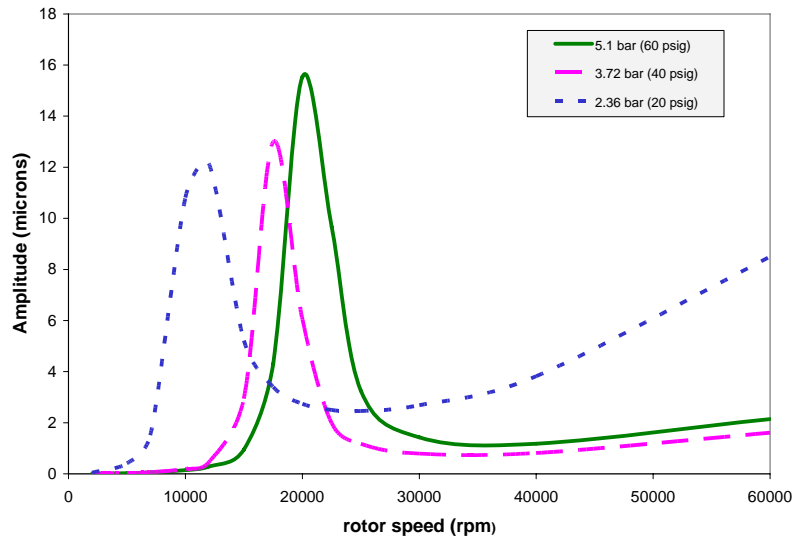**LEFT BEARING - VERTICAL PLANE Predicted response**

Fig. 15 Predicted imbalance responses for three supply pressures. Left Bearing, vertical plane. Mass imbalances distribution varies
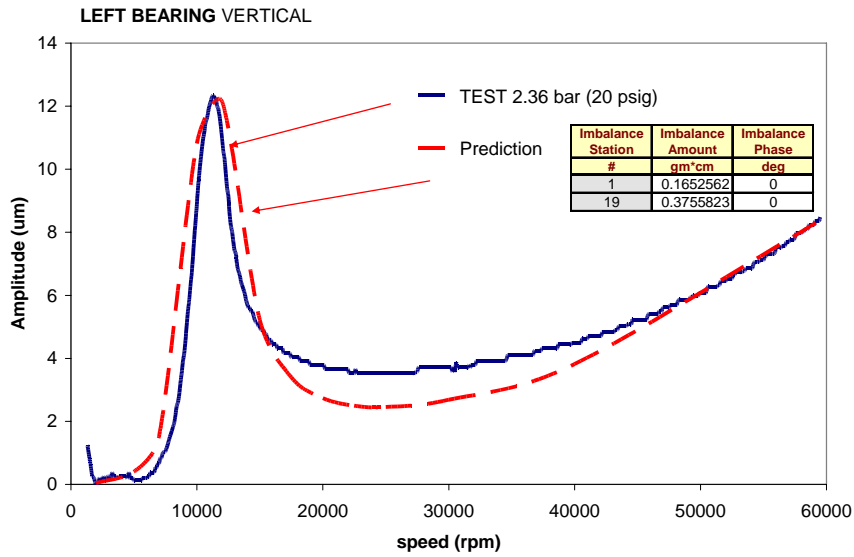

LEFT BEARING VERTICAL

Fig. 16 Comparison of predicted and measured imbalance response for supply pressure 2.36 bar (20 psig). Left Bearing, vertical plane. Mass imbalances noted